JGR Oceans

RESEARCH ARTICLE
10.1029/2019JC015960

Phase Changes of Electromagnetic Oceanic Tidal Signals

J. Saynisch-Wagner[1], J. Petereit[1], C. Irrgang[1], and M. Thomas[1,2]

[1]Earth System Modelling, Helmholtz Centre Potsdam, GFZ German Research Centre, Potsdam, Germany, [2]Institute of Meteorology, Freie Universität Berlin, Berlin, Germany

Key Points:
- Electromagnetic tidal signals show significant spatiotemporal phase changes
- Annual and monthly phase anomalies are found to be of oceanic origin
- Decadal transient phase anomalies are generated by secular variation and changing oceanic conductivity

Correspondence to:
J. Saynisch-Wagner,
saynisch@gfz-potsdam.de

Citation:
Saynisch-Wagner, J., Petereit, J., Irrgang, C., & Thomas, M. (2020). Phase changes of electromagnetic oceanic tidal signals. *Journal of Geophysical Research: Oceans*, *125*, e2019JC015960. https://doi.org/10.1029/2019JC015960

Received 11 DEC 2019
Accepted 12 MAR 2020
Accepted article online 16 MAR 2020

Abstract Over the last years, the number of studies that investigate or utilize the electromagnetic (EM) signals generated by ocean tides is steadily growing. However, the majority of these studies focuses on the amplitudes of EM tidal signals. This study investigates the phases of EM tidal signals and their changes. Twenty-six years of monthly observation-based datasets of tidal velocities, geomagnetic field, and oceanic conductivity are fed into an EM induction solver to generate varying EM tidal signals. The sensitivities of the resulting EM signals are analyzed by forbidding or allowing the input datasets to vary in time. We report on the phase's sensitivities with respect to changes in the EM properties, that is, secular variation of the geomagnetic field and changes in oceanic conductivity. Distinct temporal behavior and distinct geographic pattern for the two sensitivities can be reported. In general, apart from global phase shifts of 3–5 degrees, concentrated areas with phase shifts of up to 45 degrees occur all over the globe, over the oceans, for example, Arctic and Atlantic Ocean, as well as on coastal land regions, for example, Southwest Greenland and Japan. Very locally, phase shifts of 90 degree or higher occur.

1. Introduction

By the interaction of conducting sea water with Earth's geomagnetic field, the oceans generate and emit small electromagnetic (EM) signals. Due to their reliable detectability (Grayver & Olsen, 2019; Sabaka et al., 2016, 2018; Tyler et al., 2003), especially the electromagnetic ocean tide signals (EMOTS) have received more attention than the fields generated by the global ocean circulation. Especially since the launch of the Swarm satellite magnetometers (Friis-Christensen et al., 2006), the number of EMOTS-related studies is ever growing. Alone in the last few years, many papers studying or using EMOTS were published (Grayver & Olsen, 2019; Guzavina et al., 2018, 2019; Petereit et al., 2018, 2019; Šachl et al., 2019; Schnepf et al., 2018; Saynisch et al., 2018; Velimsky et al., 2018). EMOTS are used to infer information about the Earth's lithosphere and mantle (Guzavina et al., 2019; Grayver et al., 2017; Kuvshinov et al., 2006; Schnepf et al., 2015). Likewise, EMOTS are proposed to infer information about the oceans (Irrgang et al., 2019; Petereit et al., 2018; Saynisch et al., 2016, 2017). In addition, EMOTS influence on other EM observations, and EMOTS errors are important topics (Guzavina et al., 2018; Saynisch et al., 2018; Schnepf et al., 2014, 2018). Most of the mentioned studies focus only on the amplitudes of EMOTS and their sensitivities. However, only amplitude and phase together describe a harmonic oscillation to its full extent. A few of the mentioned studies compare amplitude and phase of EMOTS between models and observations (e.g., Grayver & Olsen, 2019; Sabaka et al., 2016; Schnepf et al., 2018). However, studies of EMOTS phase sensitivities are absent from the literature. Consequently, this study will focus on the sensitivities of the phases of EMOTS. The phases might contain additional information that are worth exploiting, too. The main question is hereby, are the EMOTS phases equally sensitive to oceanic conditions and to secular variation as the EMOTS amplitudes? (Petereit et al., 2018, 2019; Saynisch et al., 2016, 2017).

In section 2, the oceanographic datasets, the observation-based tidal velocities, and the solver for the Maxwell equations are described. Section 3 presents, compares, and discusses magnetic fields that result from the forced oceanic induction problem under different constellations of temporal variability among the input datasets. The paper closes with summary and conclusions in section 4.

2. Models and Data

In this study, the results will be exemplarily demonstrated by considering only the tide that globally emits the strongest EMOTS, the principal lunar tide M2. The M2 tide emits EMOTS of several nT and is well detectable

by spaceborne magnetometers (e.g., Grayver & Olsen, 2019; Sabaka et al., 2015, 2016; Tyler et al., 2003). Furthermore, since it is measurable outside of the ocean, the study focuses on the radial magnetic field B_z. The M2 tide oscillates with a semidiurnal period of 12 hr 25 min. The study's results can be generalized to all other oceanic tides that are related to oceanic mass transport (e.g., Sabaka et al., 2016; Saynisch et al., 2017).

Within this study, we assume that the oceanic tidal electromagnetic problem is Fourier separable, that is, that the respective induction processes can be solved in frequency space. For a single tidal frequency the induction is described by the quasi-static Maxwell equations in the following form (e.g., Kuvshinov, 2008):

$$\frac{1}{\mu_0}\nabla \times \vec{B} = \sigma^{bg}\vec{E} + \vec{J}^{ext}, \tag{1}$$

$$\nabla \times \vec{E} \;\; = -i\,\omega_{M2}\,\vec{B}, \tag{2}$$

where $\vec{B}$ is the induced magnetic field, $\vec{E}$ the induced electric field, ω_{M2} is the tidal angular frequency, σ^{bg} the electric background conductivity, μ_0 the free space magnetic permeability, $i = \sqrt{-1}$, and $\vec{J}^{ext}$ is the external electric current density which is generated by the tidal motion of sea water. $\vec{J}^{ext}$ can be considered as a periodic forcing of the induction process and is calculated by using Ohm's law in combination with the Lorentz force:

$$\vec{J}^{ext} = \sigma^{oc}(\vec{U} \times \vec{B}^{gm}), \tag{3}$$

where σ^{oc} is the conductivity of sea water, $\vec{B}^{gm}$ is the geomagnetic field, and $\vec{U}$ is the tidal oceanic transport.

The electric conductivities of the upper ocean (0–2,000 m) are calculated from oceanic temperatures and salinities of the Coriolis Ocean database for ReAnalysis (CORA5.0 Cabanes et al., 2013) by applying the Gibbs-Seawater equation (IOC et al., 2010). Here, monthly σ^{oc} fields are calculated for the time span of 1990 to 2016. Since the CORA5.0 dataset provides no values below 2,000-m depth, respective electric conductivities are taken from the World Ocean Atlas (WOA Tyler et al., 2017). In contrast to the conductivities from CORA5.0, the WOA-based conductivities are constant in time. By this approximation, a slowly changing fraction of oceanic conductance change is omitted which in part can oppose the changes originating in the upper ocean (e.g., Saynisch et al., 2016). However, the principal mechanisms of EMOTS phase changes, as discussed in this paper, are unaffected by the limitation.

For the M2 tidal transport $\vec{U}$, amplitudes and phases from the observation-based TPXO8-atlas (Egbert & Erofeeva, 2002) are used. Tidal transports are assumed constant over the study's relatively short time span of 26 years (cf., Saynisch et al., 2016).

Earth's background magnetic field $\vec{B}^{gm}$ is calculated from the likewise observation-based International Geomagnetic Reference Field (IGRF-12 Thébault et al., 2015). From this model, monthly varying fields of $\vec{B}^{gm}$ for the years 1990 to 2016 are calculated, that is, the secular variation.

All quantities are compiled on a 0.5° × 0.5° grid and are subsequently fed into equation (3) to calculate monthly varying amplitudes and phases of $\vec{J}^{ext}$ from 1990 to 2016. During the induction process (equations (1, 2)), the calculated $\vec{J}^{ext}$ amplitudes are assumed to be oscillating with a fixed M2 tidal angular frequency (ω_{M2}) that corresponds to a period of 12 hr 25 min.

To solve equations ((1, 2)), the 3D induction solver of (X3DG Kuvshinov, 2008) is used. The X3DG solver calculates magnetic fields in frequency space using a volume integral equation approach. In our configuration, a spatial varying layer for the electric background conductivity (σ^{bg}) is used. This 2D conductivity layer is the sum of ocean and sediment conductivities (Everett et al., 2003; Laske & Masters, 1997). While the ocean conductivity is spatially and temporally variable (see σ^{oc} above), the sediment conductivity is spatially variable and constant in time. Below this 2D conducting layer, a static 1D spherically symmetric mantle conductivity (Püthe et al., 2015) is used. More recent mantle conductivity models are available (Grayver et al., 2017). However, using an updated model slightly influences the depicted pattern and time series, but it will not influence the results and conclusions.

3. Results and Discussion

Again, due to the good detectability by satellite magnetometer missions, this study presents the results on the example of the radial magnetic component of the M2 EMOTS. However, the qualitative results can be applied to the other EM components and tides.

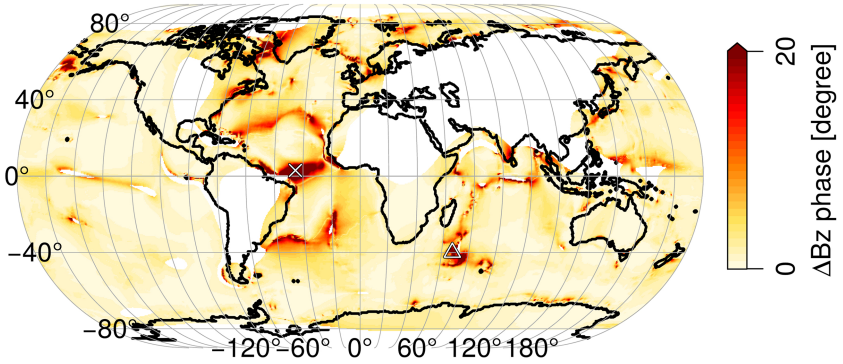

Figure 1. Maximal phase shift of the radial magnetic M2 EMOTS component within 1990 to 2016, that is, gridpoint-wise differences between the maximum of each time series and the respective minimum (modulo 360°). Phase shifts shown are calculated at sea level. Regions corresponding to M2 amplitudes below 0.3 nT, that is, 0.1 nT at satellite altitude, are omitted. The symbols (△, X) reference the locations of the time series in Figure 3.

Figure 1 shows the maximal phase shift of the calculated M2 EMOTS phase time series (see section 2), that is, the maximum of the phase time series minus the respective minimum at each grid point (modulo 360°). For a clearer plot, the phase shifts are calculated at sea level. At satellite altitude the phase shifts remain equally strong, which might be a detection advantage, however, the patches become blurry due to the inverse-squared-distance weakening of the magnetic fields. Furthermore, phase shifts are not plotted in areas where the corresponding M2 EMOTS amplitude would be below Swarm's nominal noise level at satellite altitude (0.1 nT Friis-Christensen et al., 2006).

Globally, the dataset shows phase shifts of around 3–5 degrees. In the equatorial Atlantic, Indian, and the western Pacific Ocean, phase shifts of up to 45 degrees occur. Away from the (magnetic) equator, the Bering Sea, the Labrador Sea, the North Sea, the Southwest Indian Ridge, East China Sea, and the ± 30° latitude bands of the Atlantic show similar values. Not only oceanic areas show significant phase shifts, also Southwest Greenland, Northwest America, South India, Southern Japan, and Northern Germany show comparable values. Very locally, all the mentioned areas show phase shifts of 90 degrees or higher.

The question arises, what causes the phase shifts visible in Figure 1? In this study, only two temporally variable inputs are considered, σ^{oc} and $\vec{B}^{gm}$ (see section 2). To separate the influences of these two variables on the EMOTS phases, two new experiments are performed where either σ^{oc} or $\vec{B}^{gm}$ is kept constant while the other is allowed to keep its variations. Consequently, $\vec{J}^{ext}$ has to be recalculated twice, and the Maxwell equations have to be solved again. Please remember, that σ^{oc} is also a summand of σ^{bg} in equation (1) (cf., section 2).

Analogous to Figure 1, the resultant maximal M2 phase shifts of the two experiments are plotted in Figure 2. The left panel shows the isolated effect of $\vec{B}^{gm}$ secular variation on EMOTS phase shifts. The right panel shows the isolated effect of σ^{oc} variations on EMOTS phase shifts.

By comparing the left and right panels of Figure 2, three important conclusions can be drawn. First, σ^{oc} and $\vec{B}^{gm}$ variations can both result in equally strong phase shifts. Second, with only a few exceptions, for example, the Southwest Indian Ridge, the areas are either affected by σ^{oc} or $\vec{B}^{gm}$ changes, that is, the areas are unique to the respective experiment. Third, the differences between the sum of the changes induced by σ^{oc} and $\vec{B}^{gm}$ separately and the total changes depicted in Figure 1 amount to 0.5 degrees or less (median: 0.2 degrees). Consequently, nonlinear interactions of these two sensitivities can be neglected.

The pattern in the equatorial and midlatitude Atlantic, the equatorial Indian Ocean, over South India, and in the equatorial Western Pacific Ocean are almost entirely generated by secular variation of $\vec{B}^{gm}$. Apart from the pattern over South India, these are most prominently pattern over the oceans.

Variations in σ^{oc} mostly influence areas in higher latitudes, for example, Bering Sea, Barents Sea, Laptev Sea, Southwest Greenland, North America, Japan, Iceland, and Germany. Evidently, EMOTS phases that are sensitive to oceanic conductivity can be found on land as well as in ocean regions.

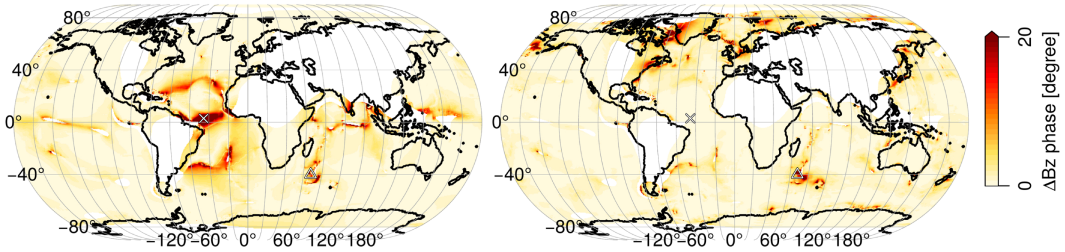

Figure 2. Maximal phase shift of the radial magnetic M2 EMOTS component within 1990 to 2016, that is, gridpoint-wise differences between the maximum of each time series and the respective minimum (modulo 360°). Phase shifts shown are calculated at sea level. Regions corresponding to M2 amplitudes below 0.3 nT, that is, 0.1 nT at satellite altitude, are omitted. Left panel: Influence of secular variation. Experiment as in Figure 1, but σ^{oc} is kept constant during the $\vec{J}^{ext}$ and σ^{bg} calculations. Right panel: Influence of oceanic conductivity variation. Experiment as in Figure 1, but $\vec{B}^{gm}$ is kept constant during the $\vec{J}^{ext}$ calculation. The symbols (△, X) reference the locations of the time series in Figure 3.

Figures 1 and 2 show the maximal range of phase changes that occur within the studied time span. For further information, a look at the phase time series is recommended.

Figure 3 compares characteristic time series of M2 EMOTS phases. The two upper time series are from the central Atlantic (see cross in Figures 1-2). These time series represent areas where EMOTS phases are sensitive to $\vec{B}^{gm}$. The lower time series are from the Southwest Indian Ridge (triangle in Figures 1-2). They represent areas where the EMOTS phase sensitives are dominated by σ^{oc}.

It becomes clear that the time series do not only differ in their sensitivities with respect to $\vec{B}^{gm}$ and/or σ^{oc}, but as a direct result of these sensitivities the time series show a very different temporal behavior. Phases which are influenced by secular variation only (Figure 3, solid lines) typically show a decadal transient behavior. Phases which are influenced by oceanic conductivity instead show monthly varying anomalies and a seasonal cycle (Figure 3, dashed lines). The oceanic conductivity itself has annual variations and respective sensitivities are recently reported for the annual cycle and EMOTS amplitudes (Petereit et al., 2019).

The phase shifts in the lower dashed line show a small decadal transient behavior, too (other areas show much larger σ^{oc} induced phase shift trends). The respective trends must be attributed to oceanic climate related processes (Saynisch et al., 2017; Petereit et al., 2019).

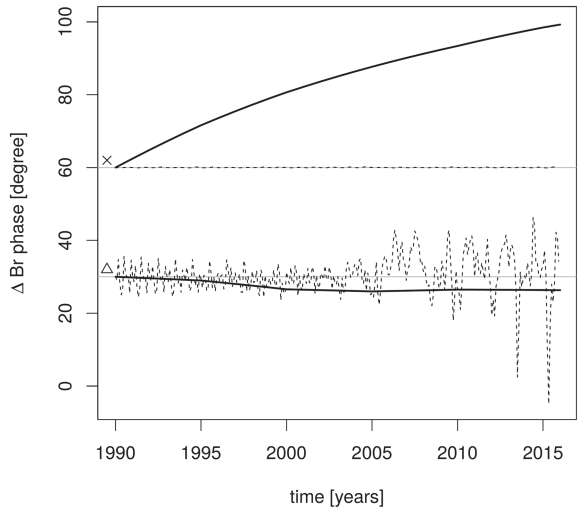

Figure 3. Phase time series of the radial magnetic M2 EMOTS component from 1990 to 2016. The two upper time series correspond to the equatorial Atlantic (see cross in Figures 1-2). The two lower time series correspond to the Southwest Indian Ridge (see triangle in Figures 1-2). Thick solid lines: Experiment as in left panel of Figure 2, that is, σ^{oc} is kept constant during the $\vec{J}^{ext}$ and σ^{bg} calculations. Thin dashed lines: Experiment as in right panel of Figure 2, that is, $\vec{B}^{gm}$ is kept constant during the $\vec{J}^{ext}$ calculation. Phases shown are calculated at sea level. To enhance the readability, an individual phase offset was added to each curve.

The Southwest Indian Ridge is sensitive to both, $\vec{B}^{gm}$ and/or σ^{oc}. However, there are many areas, like the Bering Sea, where phases are sensitive to σ^{oc} alone (compare Figure 2, left and right panels).

It is noteworthy, that the plotted pattern of σ^{oc} induced EMOTS phase changes do not exactly match the position and shape of the published pattern for σ^{oc} induced seasonal EMOTS amplitude changes (Petereit et al., 2019, Figure 2) nor the published pattern for climate change induced EMOTS amplitude changes (Saynisch et al., 2017, Figure 1). For example, EMOTS amplitudes around New Zealand are strongly sensitive to the seasonal cycle as well as oceanic climate change. The EMOTS phases in this region seem to be affected by neither. However, there is also agreement between the areas of phase and amplitude sensitivities. Most σ^{oc}-induced sensitivities are concentrated on the northern hemisphere and at least the coarse locations of phase and amplitude sensitive areas match, for example, Artic Ocean and Greenland. Still, not all areas that show σ^{oc}-sensitive amplitudes also show σ^{oc} sensitive phases and vice versa.

In reality (cf., Figure 1), the resultant phase shift time series will be a superposition of the solid and dashed lines (not shown). While the seasonal phase shifts are more or less bound to the plotted values, the transient shifts are not bound by the reported values and surely will become larger the longer the considered time span is.

Oceanic conductivity enters our approach in two places. First, in equation (3), σ^{oc} enables the generation of the electric current density $\vec{J}^{ext}$. Second, σ^{oc} influences σ^{bg} (see section 2). Consequently, in the latter case, σ^{oc} shapes the conducting system in which the electromagnetic induction takes place (see equation 1).

By using equation (3) and the composition of the 2D surface conductivity $\sigma^{bg}_{2D} = \sigma^{oc} + \sigma^{sed}$, where σ^{sed} is the conductivity of the sediments, equation (1) can be rewritten as

$$\frac{1}{\mu_0}\nabla \times \vec{B} = \sigma^{sed}\vec{E} + \sigma^{oc}_1\vec{E} + \sigma^{oc}_3\vec{U} \times \vec{B}^{gm}, \tag{4}$$

where the subscripts of σ^{oc} refer to the respective origin of σ^{oc} in equations (1) or 3. This distinction between σ^{oc}_1 and σ^{oc}_3 is entirely academic, and σ^{oc}_1 should always equal σ^{oc}_3. However, in the community, either σ^{oc}_1 or σ^{oc}_3 is treated with more care and realism, depending on the main focus of a study, for example, ocean focused or mantle focused.

To study which of the two σ^{oc} applications, σ^{oc}_1 or σ^{oc}_3, dominates the generation of the phase shifts visible in Figure 2 (right panel), two additional experiments are calculated. In both experiments, $\vec{B}^{gm}$ is kept constant.

The first experiment uses a temporally averaged σ^{oc}_1 and a temporally variable σ^{oc}_3. It represents the case where an tidally oscillating electric current density with variable amplitude forces an induction process within an environment with temporally constant conductivity.

The second experiment uses a temporally variable σ^{oc}_1 and a temporally averaged σ^{oc}_3. It represents the case where an tidally oscillating electric current density with constant amplitude forces an induction process within an environment with variable conductivity.

Figure 4 shows the maximal phase shifts of these two additional experiments. By comparing Figure 4 left and right panels, it becomes clear that most of the phase shifts caused by σ^{oc} result from the σ^{oc}_3 influence on $\vec{J}^{ext}$, that is, when σ^{oc} anomalies are multiplied by $\vec{U} \times \vec{B}^{gm}$ in Ohm's law. Significant phase shifts from the Bering Sea, Barents Sea, Laptev Sea, Greenland, North America, Japan, Iceland, and Germany occur only in the experiment with variable $\vec{J}^{ext}$ (Figure 4, left panel). When the influence of σ^{oc} is limited to Maxwell's equations and not Ohm's law, overall smaller M2 phase shifts occur (Figure 4, right panel). Respective anomalies in σ^{oc} are only amplified by $\vec{E}$.

Furthermore, all phase shift areas of the second experiment, for example, the Southwest Indian Ridge, are also phase shift areas in the first experiment, but not vice versa.

The respective phase shift time series of the two experiments are anticorrelated in most parts of the world (not shown). Consequently, in areas where both experiments show phase shifts, the two applications of σ^{oc} will dampen each other's influence on the EMOTS phases.

Again, the distinction between σ^{oc}_1 and σ^{oc}_3 is entirely academic. In reality, both effects will always occur simultaneously and equation (4) becomes

$$\frac{1}{\mu_0}\nabla \times \vec{B} = \sigma^{oc}(\vec{E} + \vec{U} \times \vec{B}^{gm}) + \sigma^{sed}\vec{E}, \tag{5}$$

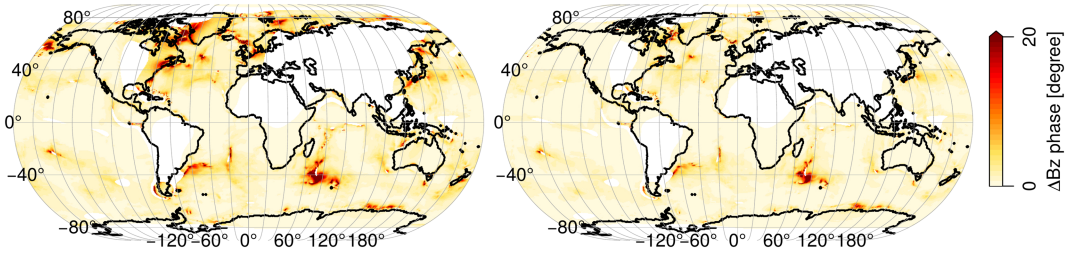

Figure 4. Maximal phase shift of the radial magnetic M2 EMOTS component within 1990 to 2016, that is, gridpoint-wise differences between the maximum of each time series and the respective minimum (modulo 360°). Phase shifts shown are calculated at sea level. Regions corresponding to M2 amplitudes below 0.3 nT, that is, 0.1 nT at satellite altitude, are omitted. Left: $\vec{B}^{gm}$ is kept constant during the $\vec{J}^{ext}$ calculation, and σ^{bg} is kept constant in addition. Right: $\vec{J}^{ext}$ is replaced by its temporal mean value, and σ^{oc} is allowed to vary σ^{bg}.

and σ^{oc} anomalies are effectively multiplied by $(\vec{E} + \vec{U} \times \vec{B}^{gm})$. However, in the community the two distinct utilizations of σ^{oc} are often not handled uniformly, and from Figure 4 the respective, small, phase errors can be derived.

A main question remains. How can variations of σ^{oc} and $\vec{B}^{gm}$ influence the phases of EMOTS? In our approach, σ^{oc} and $\vec{B}^{gm}$ are non-oscillating quantities and can therefore have neither phase nor phase shifts themselves.

We found three distinct mechanisms how variations of σ^{oc} and $\vec{B}^{gm}$ can influence the phases of EMOTS. One mechanism applies to σ^{oc} and $\vec{B}^{gm}$ changes and the other two mechanisms apply to $\vec{B}^{gm}$ changes, alone.

Mechanism I: EMOTS phase changes due to local changes in absolute strength of $\vec{J}^{ext}$ (respectively $\vec{E}$) amplitudes.

If the induction problem is considered locally isolated, for example, for a single grid point, then secular variation or σ^{oc} generated changes in the total strength of $\vec{J}^{ext}$, or changes of σ^{bg}, will result in respective changes in the local electric field strength (see equation 1). This new $\vec{E}$ field will correspond to a new induced magnetic field $\vec{B}$ (see equations (1, 2)) also of different strength. However, this amplitude change will not influence the local phases of $\vec{E}$ and $\vec{B}$.

However, the considered problem is a global induction problem and the solutions to the forced Maxwell equations, $\vec{E}$ and $\vec{B}$, depend on every location of the globe. Consequently, locally strengthening or weakening $\vec{E}$ will in turn strengthen or weaken the electric fields at other places. Likewise, the local electric field's phase will globally influence the phases of $\vec{B}$. At every single location, this could be interpreted as a weighted phase superposition of a global phase distribution, that is, a global convolution. The weights of this convolution are determined by the amplitudes in the respective source regions. Since the weights also depend on inverse squared distance, the impact will be most noticeable in the vicinity of dominant local changes.

If the argument is turned around, it becomes clear that regions with high phase changes are regions of locally weaker amplitudes, that is, regions whose EMOTS are determined or dominated by the induction in the surrounding areas. This explains, for example, the high phase changes on the magnetic equator (see Figure 1) and why the phase changes are small in areas of high amplitude sensitivity, for example, around New Zealand (Petereit et al., 2019; Saynisch et al., 2017).

Naturally, the $\vec{J}^{ext}$ phases have to be nonuniformly distributed in the beginning to have any reweighted superposition effectively impact any $\vec{B}$ field phases.

Likewise, globally uniform changes of the strength of $\vec{J}^{ext}$ amplitudes will cancel out in the convolution and will affect the phases of $\vec{E}$ and $\vec{B}$ very much less than nonuniform changes in the respective distributions (not shown).

Mechanism II: EMOTS phase changes due to local changes in $\vec{J}^{ext}$ (respectively $\vec{E}$) phases.

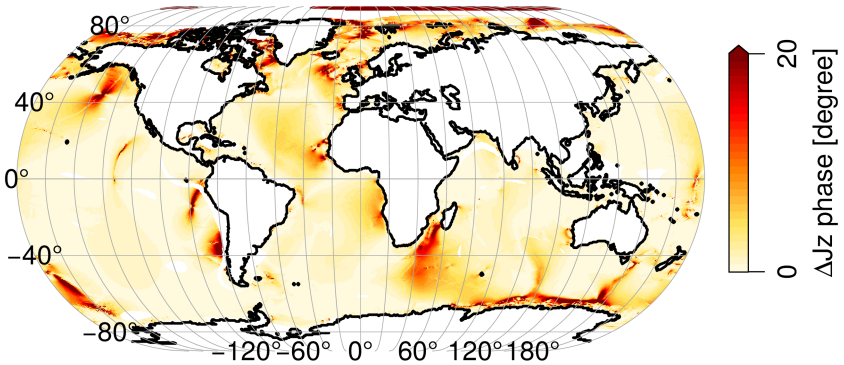

Figure 5. Maximal phase shift of the M2 radial electric current density J_z^{ext} due to secular variation within 1990 to 2016, that is, gridpoint-wise differences between the maximum of each time series and the respective minimum (modulo 360°). Phase shifts shown are calculated at sea level.

Although the geomagnetic field $\vec{B}^{gm}$ does not oscillate and therefore shows no phase shift in itself, it determines the relative weighting of $\vec{U}$ components during the generation of $\vec{J}^{ext}$ (cf., equation 3):

$$\vec{J}^{ext} \approx \vec{U} \times \vec{B}^{gm} = \begin{pmatrix} U_y B_z^{gm} - U_z B_y^{gm} \\ U_z B_x^{gm} - U_x B_z^{gm} \\ U_x B_y^{gm} - U_y B_x^{gm} \end{pmatrix}. \quad (6)$$

Please remember that the tidal transports $\vec{U}$ are the main source of oceanic tidal $\vec{B}$ oscillations. Locally, U_x, U_y, and U_z oscillate according to the traveling tidal waves. The general tidal wave pattern, that is, amplitudes and phases, are very stable in time (Saynisch et al., 2016) and are assumed constant within this study. Each tidal transport component U_x, U_y, and U_z oscillates with the same frequency but has a very different amplitude and phase distribution. Following the trigonometric identities, the superposition of the single $\vec{U}$ components in equation (6) will have recombined phases. If the weights of the components, here B_x^{gm}, B_y^{gm}, and B_z^{gm}, change due to secular variation, then the amplitude and phase distribution of the recombination will change, too.

This mechanism differs in principle from the previously explained generation of $\vec{B}$ phase shifts (Mechanism I). While the former mechanism can be seen as redistribution of static phases, this latter mechanism changes the phases of the forcing $\vec{J}^{ext}$ itself.

Vertical oceanic transports in general and vertical oceanic tidal transports in particular, that is, U_z, are assumed to be much smaller compared to their horizontal counterparts, that is, U_x, U_y. The tidal transports in this study are based on a barotropic tide model that does not include any vertical transports (see section 2). Consequently, U_z is zero and the influence of secular variation on the phases of oceanic $\vec{J}^{ext}$ can only arise in the last row of equation (6). Only there, at J_z^{ext}, two tidal transport components remain that can recombine their different phases to a new phase that depends on B_x^{gm}, B_y^{gm}. The resulting phase shifts of J_z^{ext} are plotted in Figure 5 and are of equal size to the already reported phase shifts of $\vec{B}$, that is, phase shifts of around 3–5 degrees globally, up to 45 degrees in large areas and very locally reaching 90 degrees or more.

Due to the geometry of Earth's induction system, oceanic J_z^{ext} itself has no significant influence on the induced $\vec{B}$ components. Consequently, the impact of J_z^{ext} phase changes on $\vec{B}$ phases is negligible, too. However, the phase shifts of J_z^{ext} cause phase shifts of the same size and location in $\vec{E}_z$ which might be detectable in the ocean (Larsen, 1991).

In addition, other tidal systems, for example, the ionosphere, have nonnegligible vertical transports (Schnepf et al., 2018; Yamazaki & Maute, 2017). There, the described phase change mechanism will also arise in J_x^{ext} and J_y^{ext} (if U_x and U_z, respectively, U_y and U_z differ in their phases, cf., equation 6). If so, the generated $\vec{J}^{ext}$ phase changes will significantly impact $\vec{E}$ and $\vec{B}$ phases.

Mechanism III: EMOTS phase changes due to changes in the direction (tilt) of $\vec{J}^{ext}$ (respectively $\vec{E}$) vectors.

In contrast to σ, secular variations of $\vec{B}^{gm}$ can influence each $\vec{J}^{ext}$ vector component differently (see also Mechanism II). As with Mechanism II, if the absolute strength of $\vec{J}^{ext}$ is not affected, then the local weights

of the global phase convolution will also be unaffected (Mechanism I). In addition, changes in the tilt of $\vec{J}^{ext}$ will not really change the local phases (as does Mechanism II). However, the phase's projection on the individual vector components of $\vec{B}$ will change. Consequently, and in contrast to Mechanism I, globally uniform changes in the tilt of $\vec{J}^{ext}$ will affect the EMOTS phases.

We close with some general remarks that concern all of the above mechanisms.

If the $\vec{J}^{ext}$ phases themselves (by Mechanism II) or their vector projections (by Mechanism III) change, then the phases of the surrounding areas will be affected, too. This holds true, even if the respective global convolution weights (Mechanism I) are unchanged.

Even if EMOTS amplitudes do not change at a hypothetical observation site, respective phase changes can nonetheless occur, caused by each of the above mechanisms. Consequently, observations of EMOTS phases can still reveal changes in the surrounding conduction/induction system that observations of EMOTS amplitudes cannot reveal.

In a similar manner, EMOTS phases might be used as tracers that contain information about the local EMOTS origins. For example, tidal electric currents (changes) in two distinct places might each generate the same EMOTS amplitude (change) in a third place. However, the ensuing EMOTS phase (shift) might differ.

In general, fitting a tidal mode, or any other harmonic, of fixed frequency and phase to observations that do have in fact a varying frequency or phase will lead to misinterpretations of the real amplitude. For the phase shifts described within this study, in most areas we found this effect to be below 1% on the considered time scales. Over the studied period of 26 years, the slow transient phase shifts induced by σ^{oc} and $\vec{B}^{gm}$ are not yet large enough to falsify the fits. Since very localized phase errors can exceed 90 degrees, the fitted amplitude in these areas will be very wrong. However, only in the region of the equatorial Atlantic (see Figure 1) larger areas can be found where a fixed frequency fit will underestimate the real amplitude by about 10%–30%. Of course, over longer periods, for example, 100 years, the smaller transient phase errors might become significant, too. Apart from the decadal phase shifts, the annual phase shifts induced by σ^{oc} seem to average out if whole years are considered in a potential fit.

4. Summary and Conclusions

This study focuses on the sensitivities of the electromagnetic tidal signals that are generated by the oceans. The main goal is to describe the temporal and spatial changes of tidal signal phases and their origins. Tidal transports of fixed phase and amplitude are combined with a temporal varying oceanographic conductivity and a temporal varying geomagnetic field to simulate the induced electromagnetic signals of the M2 tide. The included data have monthly resolution, cover 26 years, and are largely based on observations. The tidal transports are based on satellite altimetry; the oceanic conductivity is based on floats, buoys, expeditions, and satellite measurements; and the geomagnetic field is based on data from magnetic observatories, ground surveys, and satellite magnetometers.

The resultant M2 signals are analyzed to extract phase anomalies and their temporal development. Globally, phase shifts of around 3–5 degrees can be found. Locally, large area pattern show phase shifts of up to 45 degrees and more. Very locally, phase shifts of up to 90 degrees and more occur. The phase shifts show decadal transient behavior as well as monthly and seasonal behavior. Seasonal and monthly phase shifts have to be attributed to changes in oceanic conductivity. The decadal transient behavior can be attributed to changes of oceanic conductivity and/or changes of the geomagnetic field. While the seasonal phase shifts are basically bound to the reported values, the transient shifts will grow larger the longer the analyzed time series are. Phase shifts generated by secular variation are mostly found in the equatorial oceanic regions, especially in the Atlantic. Phase shifts generated by oceanic conductivity changes are found in higher latitudes, for example, Bering Sea, Barents Sea, Laptev Sea, and also on land, especially in Southwest Greenland and Japan.

The errors of ignoring these phase shifts by fitting tides with fixed frequencies to observations were estimated. Apart from regions of high phase shifts, for example, the equatorial Atlantic, and apart from observation time spans longer than 100 years, these errors were found to be negligible.

The presented EMOTS phase changes can either be the result of a temporal varying redistribution of fixed local phases or a result of temporal changes in the local phase's projection on a fixed coordinate system. An

additional mechanism is described that indeed changes the local phases of oceanic electric current densities. However, the affected electric current density component significantly influences only the radial electric field and not the oceanic magnetic fields. In a follow-up study one should analyze the impact of the latter mechanism in a tidal system that has significant vertical transports, for example, the ionosphere.

A few characteristics of EMOTS phases emerged which might complement the information usually drawn from EMOTS amplitudes. At satellite altitude the phase shifts are as strong as on the Earth's surface, which might be a detection advantage. Even if EMOTS amplitudes do not change at an observation site, phase changes can still occur and reveal changes in the surrounding conduction/induction system to which the local amplitudes are not sensitive to. EMOTS phases might be used as tracers that contain information about the local EMOTS amplitude's geographical origins.

These properties highly recommend EMOTS phases for further study, especially in observations.

Acknowledgments
This study has been funded by the German Research Foundation (SPP1788, Dynamic Earth) and the Initiative and Networking Fund of the Helmholtz Association through the project "Advanced Earth System Modelling Capacity (ESM)." The authors thank for the opportunity to use data from the World Ocean Atlas (www.nodc.noaa.gov/OC5/woa13/), the TPXO tidal model (volkov.oce.orst.edu/tides/), the CORA ocean reanalysis dataset (www.coriolis.eu.org/), the IGRF-12 geomagnetic reference field (www.ngdc.noaa.gov/IAGA/vmod/igrf.html), and facilities from the German High Performance Computing Centre for Climate and Earth System Research (www.dkrz.de). We thank Alexey Kuvshinov (kuvshinov@erdw.ethz.ch) for the opportunity to use the 3D EM induction solver X3DG. We thank Zdenek Martinec and Yosuke Yamazaki for fruitful discussions. We thank Neesha Schnepf and one anonymous reviewer for their assistance on this manuscript.

References

Cabanes, C., Grouazel, A., von Schuckmann, K., Hamon, M., Turpin, V., & Coatanoan, C. (2013). The CORA dataset: Validation and diagnostics of in-situ ocean temperature and salinity measurements. *Ocean Science*, *9*, 1–18.

Egbert, G. D., & Erofeeva, S. Y. (2002). Efficient inverse modeling of barotropic ocean tides. *Journal of Atmospheric and Oceanic Technology*, *19*, 183–204.

Everett, M. E., Constable, S., & Constable, C. G. (2003). Effects of near-surface conductance on global satellite induction responses. *Geophysical Journal International*, *153*(1), 277–286.

Friis-Christensen, E., Lühr, H., & Hulot, G. (2006). Swarm: A constellation to study the Earth's magnetic field. *Earth Planets Space*, *58*(4), 351–358.

Grayver, A. V., Munch, F. D., Kuvshinov, A. V., Khan, A., Sabaka, T. J., & Tøffner-Clausen, L. (2017). Joint inversion of satellite-detected tidal and magnetospheric signals constrains electrical conductivity and water content of the upper mantle and transition zone. *Geophysical Research Letters*, *44*, 6074–6081. hppts://doi.org/2017GL073446

Grayver, A. V., & Olsen, N. (2019). The magnetic signatures of the M_2, N_2, and O_1 oceanic tides observed in Swarm and CHAMP satellite magnetic data. *Geophysical Research Letters*, *46*, 4230–4238. https://doi.org/10.1029/2019GL082400

Guzavina, M., Grayver, A., & Kuvshinov, A. (2018). Do ocean tidal signals influence recovery of solar quiet variations? *Earth Planets Space*, *70*(1), 5.

Guzavina, M., Grayver, A., & Kuvshinov, A. (2019). Probing upper mantle electrical conductivity with daily magnetic variations using global-to-local transfer functions. *Geophysical Journal International*, *219*(3), 2125–2147.

IOC, SCOR, & APSO (2010). The international thermodynamic equation of seawater - 2010: Calculation and use of thermodynamic properties.

Irrgang, C., Saynisch, J., & Thomas, M. (2019). Estimating global ocean heat content from tidal magnetic satellite observations. *Scientific Reports*, *9*(7893), 8.

Kuvshinov, A. V. (2008). 3-D global induction in the oceans and solid Earth: Recent progress in modeling magnetic and electric fields from sources of magnetospheric, ionospheric and oceanic origin. *Surveys in Geophysics*, *29*(2), 139–186.

Kuvshinov, A., Junge, A., & Utada, H. (2006). 3-D modelling the electric field due to ocean tidal flow and comparison with observations. *Geophysical Research Letters*, *33*, L06314. https://doi.org/10.1029/2005GL025043

Larsen, J. C. (1991). Transport measurements from in-service undersea telephone cables. *IEEE Journal of Oceanic Engineering*, *16*(4), 313–318.

Laske, G., & Masters, G. (1997). A global digital map of sediment thickness. *Eos, Transactions American Geophysical Union*, *78*, 46. Fall Meet. Suppl.

Petereit, J., Saynisch, J., Irrgang, C., & Thomas, M. (2019). Analysis of ocean tide induced magnetic fields derived from oceanic in-situ observations: Climate trends and the remarkable sensitivity of shelf regions. *Journal of Geophysical Research: Oceans*, *124*, 8257–8270. https://doi.org/10.1029/2018JC014768

Petereit, J., Saynisch, J., Irrgang, C., Weber, T., & Thomas, M. (2018). Electromagnetic characteristics of ENSO. *Ocean Science*, *14*(3), 515–524.

Püthe, C., Kuvshinov, A., Khan, A., & Olsen, N. (2015). A new model of Earth's radial conductivity structure derived from over 10 yr of satellite and observatory magnetic data. *Geophysical Journal International*, *203*(3), 1864–1872.

Sabaka, T. J., Olsen, N., Tyler, R. H., & Kuvshinov, A. (2015). CM5, a pre-Swarm comprehensive geomagnetic field model derived from over 12 yr of CHAMP, Orsted, SAC-C and observatory data. *Geophysical Journal International*, *200*(3), 1596–1626.

Sabaka, T. J., Toffner-Clausen, L., Olsen, N., & Finlay, C. C. (2018). A comprehensive model of Earth's magnetic field determined from 4 years of Swarm satellite observations. *Earth Planets Space*, *70*(130), 26.

Sabaka, T. J., Tyler, R. H., & Olsen, N. (2016). Extracting ocean-generated tidal magnetic signals from Swarm data through satellite gradiometry. *Geophysical Research Letters*, *43*, 3237–3245. https://doi.org/10.1002/2016GL068180

Šachl, L., Martinec, Z., Velimsky, J., Irrgang, C., Petereit, J., & Saynisch, J. (2019). Modelling of electromagnetic signatures of global ocean circulation: Physical approximations and numerical issues. *Earth Planets Space*, *71*(1), 58.

Saynisch, J., Irrgang, C., & Thomas, M. (2018). Estimating ocean tide model uncertainties for electromagnetic inversion studies. *Annals of Geophysics*, *36*(4), 1009–1014.

Saynisch, J., Petereit, J., Irrgang, C., Kuvshinov, A., & Thomas, M. (2016). Impact of climate variability on the tidal oceanic magnetic signal—A model based sensitivity study. *Journal of Geophysical Research: Oceans*, *121*, 5931–5941. https://doi.org/10.1002/2016JC012027

Saynisch, J., Petereit, J., Irrgang, C., & Thomas, M. (2017). Impact of oceanic warming on electromagnetic oceanic tidal signals: A CMIP5 climate model-based sensitivity study. *Geophysical Research Letters*, *44*, 4994–5000. https://doi.org/10.1002/2017GL073683

Schnepf, N. R., Kuvshinov, A., & Sabaka, T. (2015). Can we probe the conductivity of the lithosphere and upper mantle using satellite tidal magnetic signals? *Geophysical Research Letters*, *42*, 3233–3239. https://doi.org/10.1002/2015GL063540

Schnepf, N. R., Manoj, C., Kuvshinov, A., Toh, H., & Maus, S. (2014). Tidal signals in ocean-bottom magnetic measurements of the Northwestern Pacific: Observation versus prediction. *Geophysical Journal International*, *198*(2), 1096–1110.

Schnepf, N. R., Nair, M., Maute, A., Pedatella, N. M., Kuvshinov, A., & Richmond, A. D. (2018). A comparison of model-based ionospheric and ocean tidal magnetic signals with observatory data. *Geophysical Research Letters*, *45*, 7257–7267. https://doi.org/10.1029/2018GL078487

Thébault, E., Finlay, C. C., Beggan, C. D., Alken, P., Aubert, J., & Barrois, O. (2015). International geomagnetic reference field: The 12th generation. *Earth Planets Space*, *67*(1), 79.

Tyler, R. H., Boyer, T. P., Minami, T., Zweng, M. M., & Reagan, J. R. (2017). Electrical conductivity of the global ocean. *Earth Planets Space*, *69*(1), 156.

Tyler, R. H., Maus, S., & Luhr, H. (2003). Satellite observations of magnetic fields due to ocean tidal flow. *Science*, *299*(5604), 239–241.

Velimsky, J., Grayver, A., & Kuvshinov, A. (2018). On the modelling of M2 tidal magnetic signatures: Effects of physical approximations and numerical resolution. *Earth Planets Space*, *70*, 192.

Yamazaki, Y., & Maute, A. (2017). Sq and EEJ—A review on the daily variation of the geomagnetic field caused by ionospheric dynamo currents. *Space Science Reviews*, *206*(1), 299–405.